In silico model of a patient specific Aorta using 4D-MRI data simulating the hemodynamic effects of mechanical aortic valve

Bongert M. [1], Geller M. [1], Pennekamp W. [2], Nicolas V. [2]
[1] Fachhochschule Dortmund, Forschungsschwerpunkt „BioMedizinTechnik“, Dortmund, Deutschland
[2] Ruhr-Universität Bochum, Universitätsklinikum Bergmannsheil, Institut für Diagnostische Radiologie, Interventionelle Radiologie und Nuklearmedizin, Bochum, Deutschland

bongert@fh-dortmund.de

Introduction

In 2010, approximately 11,500 patients in Germany received surgical replacement of the aortic valve as a result of heart valve disease. To date, surgeons have lacked a tool for pre-operatively assessing the impact and subsequent effectiveness of aortic valve implant location in individual patients.

Methods

The individual anatomy of the aorta was captured using magnetic resonance imagining (MRI) and contrast-rich gradient echo resonance with Bright Blood Display (TRUE-FISP – True Fast Imaging With Steady Precession). 4D-DICOM data was first split into the individual 3-D blocks before segmentation and conversion to a CAD format (Mimics). Numerical simulation was based on patient geometry and the physiology of the parameters displayed. This work-flow generated, personalized simulation model was used for a systematically and virtual investigation of the effect of valve site on blood flow in a healthy 42 year subject.

Results

The valve caused turbulence with reflux in the *bulbus*, the intensity and distribution of which depended on valve location. Furthermore, characteristic for these valves, two velocity traces where observed extending into the aortic arch, the positions of which also depended on valve site. Individual implant sites resulted in raised but haemolytically non-critical values ($\tau crit=425Pa$) for wall shear stress at the exit of the *bulbus*. The computer model was validated by MRI (peak velocity).

Conclusion

Implantation of an aortic valve as an image guided intervention offers improved planning and prognosis when 4-D imaging (MRT) is combined with numerical simulation for a patient-specific computer model.
The ante- and retrograde flow resulting from mechanical aortic valve implantation reported in this study was confirmed by Pennekamp et al.
In stationary simulations, aortic elasticity and valve leaflet movement were not considered, and it was not possible to make any conclusions about the dynamic effects such as jet streaming, Windkessel effect and cavitation.

Imaging in Radiotherapy

U.Haverkamp, H.T.Eich

University of Münster, Department of Radiotherapy

Radiotherapy lies on medical imaging to determine the extent of disease, building a 3D-model to calculate the dose distribution and as "on board imaging" to confirm a match of treatment set up to the planned treatment. The basic tool in preplanning imaging is computed tomography (100%), followed by magnetic resonance imaging (15%) and positron emission tomography (10%), the numbers relate to the University of Münster. In the management of organ motion a 4D-imaging is necessary, realized as 4D-CT or list mode (PET).

The "on board imaging" underwent a development from planar imaging to scanning techniques, from MV to kV. Today deviations in the setup can be corrected automatically and physiological changes can lead to recalculations of treatment plans. The conventional radiotherapy has changed to online image guided adaptive radiotherapy. Medical physicists are concerned with different areas: The image acquisition and analysis is still not optimal, the necessary X-ray exposure and the radiobiological significance of the kV imaging is not yet clear and the quality assurance is under discussion.

A particular challenge to the on-board imaging is the detection of organ motion, this can be done via the 4D computed tomography or respiratory triggering. With the increasing establishment of hypofractionated schemes, the importance of this task continues to increase.

The integration of other imaging modalities in therapy equipments is on its way. A few installations with a combination of radiotherapy delivery and simultaneous MRI, PET online control during heavy-ion treatment or telerobotic ultrasound systems for realtime detection of target motion already exist.

Artifact simulation and measurement of interventional needles in MR imaging

Morwan Choli[1], Sebastian Schmitt[2], Katharina Skopnik[1], Gregor Schaefers[1]
[1]MR:comp GmbH, Testing Services for MR Safety & Compatibility, Gelsenkirchen, Germany, choli@mrcomp.com
[2]Medical Engineering Laboratory, Westphalian University of Applied Sciences, Gelsenkirchen, Germany

Introduction

Needle navigation and visibility in magnetic resonance imaging (MRI) is a challenging issue due to image artifacts in the surroundings of the needle which are usually much larger than the real dimensions of the object. Depending on image sequence selection and field strength of MR-systems, artifacts change in size and shape significantly. Especially if deseased tissue is smaller than the image artifacts a biopsie can not be performed easily. Following work shows simulations of needle artefacts which are in good agreement with real measurements.

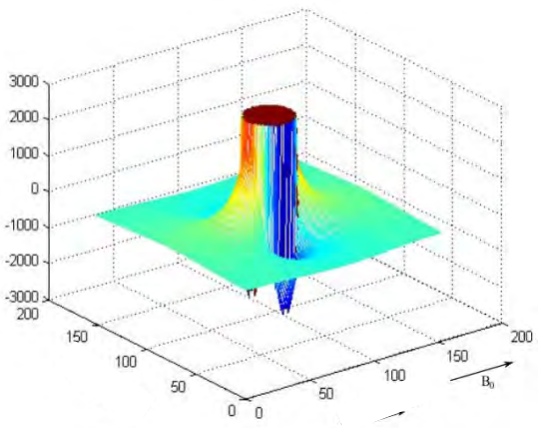

Figure 1: Frequency distribution around a biopsy needle due to susceptibility differences of needle material and surrounding tissue. Frequencies are relative to the Larmorfrequence $\omega_0=\gamma B_0$

Methods

For simulating image artifacts Bloch-Equations were implemented using the Matlab programming language (MathWorks, Natick, MA). First the phase distribution around a capilar which represents the cross section of a biopsy needle were simulated to get the field distortions around the object which are dependent on susceptibility differences of the needle material and surrounding tissue. Using different boundary conditions enables simulation of different imaging-sequences.

Results

Figure 1 shows frequency distribution around a needle cross section due to susceptibility differences of needle material and surrounding tissue. Simulated frequencies were always relative to the Larmorfrequence $\omega_0=\gamma B_0$. This distribution were used to simulate MRI-sequences with different boundary conditions and signal behaviour like (a) bSSSP (balanced steady state free precession, also called TrueFISP/FIESTA) and (b) FLASH[1] imaging sequences. Figure 2 shows simulated bSSFP data. The simulated absolute value shown in (a) and imagephase in (b). Coresponding measred data is shown in Fig. 2 (c) and (d) for the absolute value and image phase.

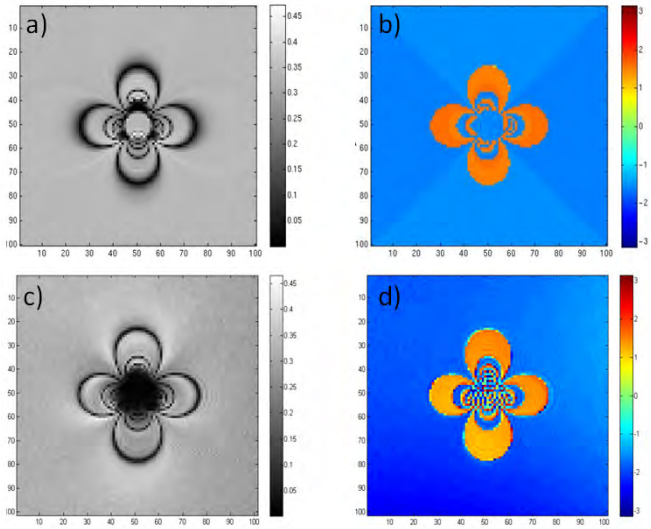

Figure 2: bSSFP Simulations and measurements. (a) simulated absolute image and image phase shown in (b). Corresponding experiments (c) and (d).

Conclusion

Results show a good agreement between simulated and measured data. With developed tools previous calculations and simulations can be done to evaluate easily size and shape of MR-artifacts. Further development of the simulations could include simulation of RF-induced artifacts. Also noise levels could be implemented to forecast overall image quality including signal intensity as well.

References

1. A. Haase, et al. (1986). *Journal of Magnetic Resonance* **67** (2): 258–266.

Acknowledgement

The authors acknowledge the IuK Gender Med.NRW program (grant no. 005-GW02-052) and the Federal State North-Rhine Westphalia for financial support.

Biomed Tech 2014; 59 (s1) © 2014 by Walter de Gruyter • Berlin • Boston. DOI 10.1515/bmt-2014-4205

Marker Clip Detection in Ultrasound Receive Raw Data

P Holzmann[1], A Poelstra[2] and H M Overhoff[2]
[1]School of Life Sciences FHNW, Muttenz, Switzerland
[2]Medical Engineering Laboratory, Westphalian University of Applied Sciences, Gelsenkirchen, Germany,
heinrich-martin.overhoff@w-hs.de

Abstract

Clips are used to mark relevant tissue regions. In some cases, these clips are poorly visible in ultrasound images. A combined image and receive raw data analysis shall assign data subsamples to classes "clip" and "tissue". In a supervised learning procedure, suitable features were determined. The classificator primarily rates the pass and stop band characteristics of the raw data's Fourier amplitude spectra. Classification could be performed with specifity ≈ 0.98 and sensitivity ≈ 0.30.

Figure 1: U-shaped clip with length × width × height $\approx 5\,\text{mm} \times 5\,\text{mm} \times 1\,\text{mm}$ used in this study.

1 Introduction

Clips are used to mark important regions in tissue. For example, clips are used in marking tumour tissue for radiation planning or core biopsy sites. Especially during diagnsotics, they are implanted minimally invasive percutaneously through soft tissue using a needle-shaped one-way applicator. Some clip have a shape memory alloy and get back to its former shape after injection (Figure 1).

A lot of anatomical structures reflect ultrasound waves. In conventional image reconstruction, e.g. a delay- and sum-procedure, clips and anatomical structures are visualized similarly. In such cases, the visibility of clips in ultrasound images is limited and their localization demands high skills of the physician.
Due to the clip's texture it seems likely that their reflected soundwaves, and therefore the summed receive raw data (A-lines), present typical features. It is assumed, that such features can be exploited to improve clip visualization. It is hypothesized that clip-typical features can be extracted from Fourier spectra of receive raw data.

2 Material and Methods

2.1 Material

Clips were injected into a porc liver phantom. Only orthogonal that part of the clip, which is orthogonal to sound wave propagation. Furthermore, the analysis was restricted to images which did show almost the entire clip.

For acquisition of raw data $\hat{s}(i)$ an Esaote MyLab70 XVG ultrasound scanner with mechanical 3-D linear transducer LA523 and research interface ART.LAB was used. An image acquisiton consists of $N_\mathrm{I} \times N_\mathrm{J}$ sample pixels ($N_\mathrm{I} = 2033, N_\mathrm{J} = 363$), and the reconstructed image $\boldsymbol{G}$ can be noted as $N_\mathrm{I} \times N_\mathrm{J}$ matrix.
Its scalar gray scale values are in the range $0 \leq g \leq 255$.
One A-Linie corresponds to one image column j.

2.2 Methods

A method for the classification of windowed A-line samples $\hat{s}(i)$ into the classes "clip" and "tissue" is presented. It can be divided in an image based and a raw data based analysis.

2.2.1 Image Analysis

The envelope of a time-continuous signal $s(t)$ can be determined by its Hilbert transform

$$\mathcal{H}\{s(t)\} = \frac{1}{\pi} \int_{-\infty}^{\infty} \frac{s(t)}{t-\eta} d\eta. \qquad (1)$$

Let index i_0 refer to the suspected position of the clip. Because clips impose by their high reflectivity, i_0 is de-

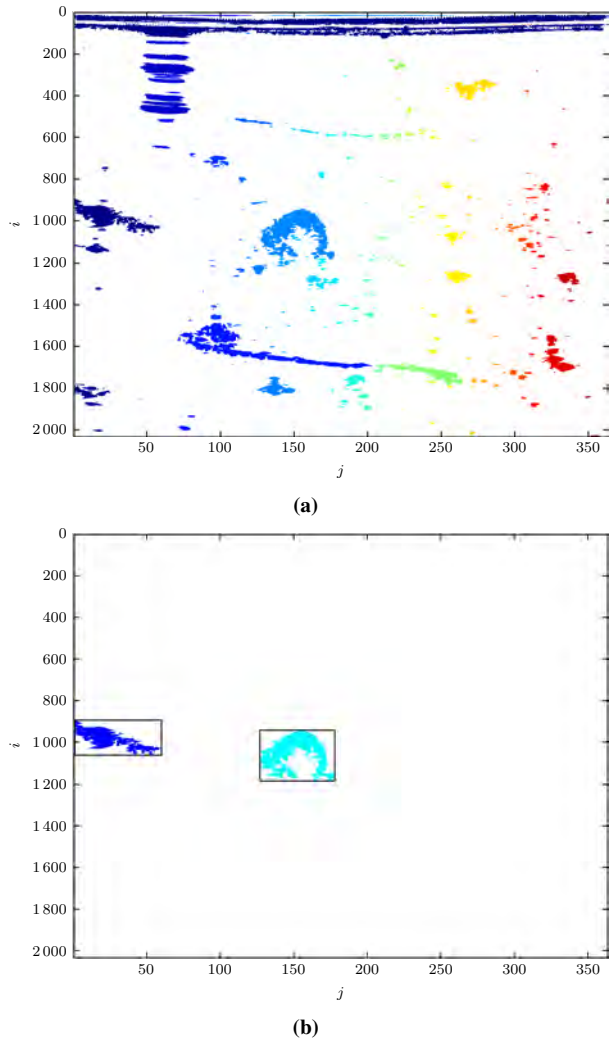

Figure 2: (a) Blobs after binarization and (b) large blobs with rectangle.

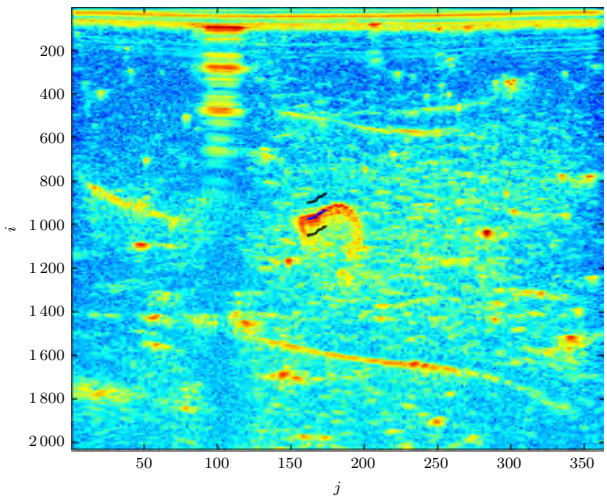

Figure 3: Clip signal subsets visualized as upper and lower line black lines. The middle line represents i_0.

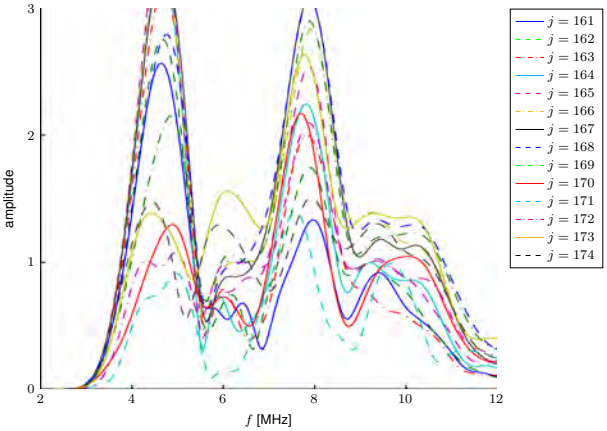

Figure 4: Fourier amplitude spectra of clip signal subsamples $\hat{s}$ for different A-lines (index j).

fined by the amplitude relation

$$\mathcal{H}\{\hat{s}(i_0)\} \geq \mathcal{H}_{\text{thres}}. \tag{2}$$

The image is binarized with this amplitude threshold. Adjacent pixels are morphologically pooled to a "blob". The blobs are labelled in the order of their number of pixels. Blobs with high labels are enclosed by a rectangle. Its aspect ratio is determined and decides, if the blob's measures fit to those of a clip (Figure 2). In this case, index i_0 is kept and a receive signal analysis is performed.

2.2.2 Raw Data Analysis

Subsamples of the receive signal $\hat{s}(i)$ are further analyzed:

$$i_0 - \Delta\tau \leq i \leq i_0 + \Delta\tau. \tag{3}$$

Such subsamples are finally convoluted with a Hanning-window.

The discrete time span $2 \cdot \Delta\,\tau + 1$ is assumed to contain those signal part which allows for proper feature definition (Figure 3).

Figure 4 shows, that the Fourier amplitude spectra have a pass - stop - pass band character, and each of the bands is narrow. Because the high frequency pass band characteristics may severely depend on frequency dependent absorption [2], only the low frequency pass band and stop band characteristics shall be used for feature definition:

$$\begin{aligned} f_1 &= \text{true, if } S_{\text{low}}^{\text{pass}} \leq S(f) \leq S_{\text{high}}^{\text{pass}} \text{ for } f_{\text{low}}^{\text{pass}} \leq f \leq f_{\text{high}}^{\text{pass}} \\ f_2 &= \text{true, if } S_{\text{low}}^{\text{stop}} \leq S(f) \leq S_{\text{high}}^{\text{stop}} \text{ for } f_{\text{low}}^{\text{stop}} \leq f \leq f_{\text{high}}^{\text{stop}} \end{aligned} \tag{4}$$

2.2.3 Expert vs. feature based classification

A feature based classification intends to assign an object to one of two classes. Such an assignment can be noted in a fourfold table 1 [1]. It demonstrates the number coincidences between manually performed expert and feature based automatic classification.

		expert classification	
		$k_\mu = +1$	$k_\mu = -1$
classifyer result	$\tilde{k}_\mu = +1$	N_{TP}	N_{FP}
	$\tilde{k}_\mu = -1$	N_{FN}	N_{TN}

Table 1: Fourfold table with expert vs. classifier rating cases and numbers of coincidences.

Here, the object is the signal $\hat{s}(i)$ at time span (3), and the classes are "clip" ($\tilde{k} = +1$) and "tissue" ($\tilde{k} = -1$). The features are taken from $\hat{s}(i)$ and the amplitude of its Fourier spectrum $S(f)$. The parameters $\mathcal{H}_{\mathrm{thres}}, \Delta\tau, S_{\mathrm{low}}^{\mathrm{pass}}, S_{\mathrm{high}}^{\mathrm{pass}}, f_{\mathrm{low}}^{\mathrm{pass}}, f_{\mathrm{high}}^{\mathrm{pass}}, S_{\mathrm{low}}^{\mathrm{stop}}, S_{\mathrm{high}}^{\mathrm{stop}}, f_{\mathrm{low}}^{\mathrm{stop}}, f_{\mathrm{high}}^{\mathrm{stop}}$ have to be chosen to maximize specificity.

3 Results

In a first enumeration, the parameters

$$\mathcal{H}_{\mathrm{thres}} = 130,$$
$$\Delta\tau = 75,$$
$$S_{\mathrm{low}}^{\mathrm{pass}} = 1,$$
$$S_{\mathrm{high}}^{\mathrm{pass}} = 4,$$
$$f_{\mathrm{low}}^{\mathrm{pass}} = 3.7\,\mathrm{MHz},$$
$$f_{\mathrm{high}}^{\mathrm{pass}} = 5.0\,\mathrm{MHz},$$
$$S_{\mathrm{low}}^{\mathrm{stop}} = 0,$$
$$S_{\mathrm{high}}^{\mathrm{stop}} = 1,$$
$$f_{\mathrm{low}}^{\mathrm{stop}} = 5.5\,\mathrm{MHz},$$
$$f_{\mathrm{high}}^{\mathrm{stop}} = 6.5\,\mathrm{MHz}$$

did show classification with a sensitivity ≈ 0.30 and specifity ≈ 0.98. Exemplary, Figure 5 shows the classification in one image. True-negative pixels are not shown due to their high number, the image is presented instead.

4 Discussion

The presented method of combined image and signal processing could predict clip signal subsamples in receive raw data with an extremely high specifity at an acceptable sensitivity. The enumeration was chosen to, as it allows ROC curve based analyses on the robustness of the parameters.
The derived classificatory has band pass character, which coincides with the transmit dynamics of the transducer. Due to the experimental setup, highest reflection amplitudes could be assumed. Therefore, the amplitude threshold $\mathcal{H}_{\mathrm{thres}}$ might be a classification parameter which is of limited external validity.
Future work is addressed to the detection of clips in oblique positions in order to investigate, if blob dimensions and amplitude threshold persist being reliable classification parameters.

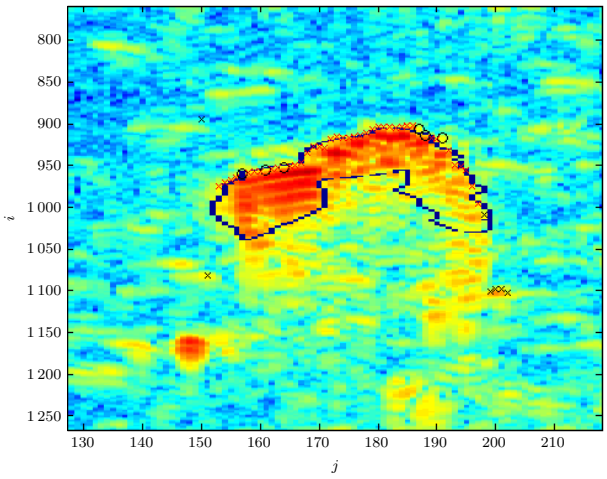

Figure 5: Classification result. black x = false-positive, black o = false-negative, and red x = true-positive.

Acknowledgement

This work was funded by the Federal Ministry of Education and Research in the FHprofUnt 2012 program, grant no. 03FH041PX2.

References

[1] Tom Fawcett. ROC graphs: Notes and practical considerations for data mining researchers. Technical report, HP Laboratories, Palo Alto, CA, USA, 2003. Stand: 29. Juli 2013.

[2] A. Poelstra and H.M. Overhoff. Determination of the depth dependent Fourier spectra of catheter reflections for automatic catheter detection. In *IEEE International Ultrasonics Symposium (IUS)*, pages 284 –287, oct. 2011.

Raw Data Compression in Magnetic Resonance Imaging

S Schmitt[1] and H M Overhoff[1]
[1]Medical Engineering Laboratory, Westphalian University of Applied Sciences, Gelsenkirchen, Germany, sebastian.schmitt@w-hs.de

Abstract

For MR-guided interventions with real-time monitoring of the needle position, a reduced the scan time is necessary. The conflict between acquisition duration demands for high image quality and fast imaging can be overcome by compressed sensing, i.e. by acquisition of only the "relevant" measurements. Here, these relevant measurements are determined by finding a sparse representation of the measured signal by solving a constrained optimization problem. This optimization problem has been solved for different synthetically generated **k**-space data and its practical relevance is discussed.

1 Introduction

MR-guided interventions (e.g. biopsies) are conceptually possible, if the duration for imaging the region of interest allows for controlling the needle position in real-time. High resolution MR images require a large quantity of acquired **k**-space data. The conflict between acquisition duration demands for high image quality and fast imaging can be overcome by compressed sensing, i.e. by acquisition of only the "relevant" measurements. Therefore, the task is to determine that small part of the measurement data which is required to reconstruct an image but not significantly losing information content of the original signal or losing image quality. Images are usually noted as matrix $\mathbf{G}$ of size $N_\mathrm{I} \times N_\mathrm{J}$. For the following analysis it is helpful to note them as vectors $\mathbf{g}$, which are the concatenations of the columns of $\mathbf{G}$. Their sizes are $n \times 1 = N_\mathrm{I}N_\mathrm{J} \times 1$. The same holds for the $N_\mathrm{I} \times N_\mathrm{J}$ signal matrix $\mathbf{K}$ and its $N_\mathrm{I}N_\mathrm{J} \times 1$ vector notation $\mathbf{k}$.
The most important and at the same time smallest part of the **k**-space can be defined to be the ℓ_0-norm approximation of the measurement vector $\mathbf{k}$. This procedure is known as finding a sparse representation $\widetilde{\mathbf{k}}$ of the measured signal $\mathbf{k}$ by solving a constrained inverse problem [2]. The solution to this optimization problem is a **k**-space vector $\widetilde{\mathbf{k}}$ with minimum ℓ_0-norm which can be reconstructed to an approximated image $\widetilde{\mathbf{g}}$ with an appropriate relative approximation error r_ε.
The relation between compression rate r_c and relative approximation error r_ε shall be derived at the example of different MR images. For tolerable relative approximation errors r_ε it shall be investigated, if practicable acquisition **k**-space trajectories are possible.

2 Material and Methods

2.1 Material

In magnetic resonance imaging, raw data $\mathbf{K}$ and image $\mathbf{G}$ are linked via the 2D-Fourier transform

$$\mathbf{K} = \mathcal{F}\{\mathbf{G}\}. \tag{1}$$

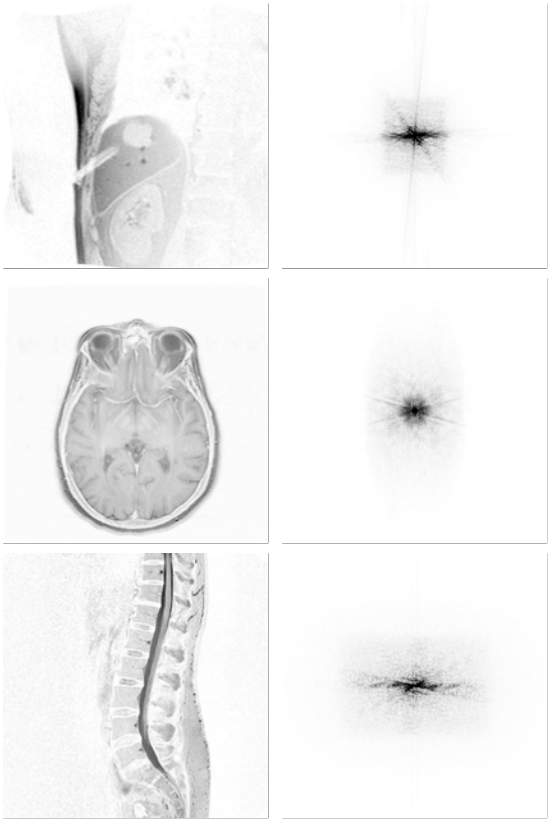

Figure 1: Gray scale inverted images $\mathbf{g}_{1-3}$ and their corresponding synthetically generated raw data $\mathbf{k}_{1-3}$ in logarithmic representation.

Therefore, raw data can be approximately generated synthetically by applying the 2D-Fourier transform to an image. In Figure 1 three images and their corresponding synthetically generated raw data (**k**-spaces) are shown.

Due to the coincidence of the ℓ_0- and the ℓ_1-norm minimum under certain conditions [2], the optimization problem of minimizing the ℓ_0-norm of the data vector $\mathbf{k}$ is solved with the MATLAB-toolbox ℓ_1-magic [1].

2.2 Methods

2.2.1 ℓ_1-norm and ℓ_0-norm

Reducing the quantity of acquired $\mathbf{k}$-space data can be expressed as minimizing the ℓ_0-norm of the $\mathbf{k}$-space vector $\mathbf{k}$. The ℓ_0-norm of a vector $\mathbf{k}$ is defined as its number of non-zero elements

$$\|\mathbf{k}\|_0 = |i : k_i \neq 0| \,. \tag{2}$$

The vector $\widetilde{\mathbf{k}}$ with minimum ℓ_0-norm needs to comply with a minimum approximation error $\varepsilon = \|\mathbf{g} - \widetilde{\mathbf{g}}\|_2$ between the approximated image $\widetilde{\mathbf{g}}$, reconstructed from the reduced $\mathbf{k}$-space data, and the original image $\mathbf{g}$. Therefore, the non-convex optimization problem

$$\widetilde{\mathbf{k}} = \min_{\mathbf{k}} \|\mathbf{k}\|_0 \text{s.t.} \, \|\mathbf{g} - \widetilde{\mathbf{g}}\|_2 \leq \varepsilon, \tag{3}$$

needs to be solved. In [2] is shown that under certain conditions the solution to the problem in (3) is equal to the solution to the convex optimization problem

$$\widetilde{\mathbf{k}} = \min_{\mathbf{k}} \|\mathbf{k}\|_1 \text{s.t.} \, \|\mathbf{g} - \widetilde{\mathbf{g}}\|_2 \leq \varepsilon, \tag{4}$$

with the ℓ_1-norm

$$\|\mathbf{k}\|_1 = \sum_{i=1}^{n} |k_i|. \tag{5}$$

2.2.2 ℓ_1-norm minimization with ℓ_1-magic

The MATLAB-toolbox ℓ_1-magic [1] can solve ℓ_1-norm minimization problems. It provides code which can be modified in order to adapt the algorithms to the specific optimization problem. The application of ℓ_1-magic as a solver for the optimization problem (4) yields a vector $\widetilde{\mathbf{k}}$ with minimum ℓ_1-norm. However, this vector may contain elements which are only close to zero: $\widetilde{k}_i \approx 0$. Therefore, a threshold k_{th} is applied to the vector $\widetilde{\mathbf{k}}$ such that the ℓ_0-norm is approximately minimized as well. The result is a vector $\widetilde{\mathbf{k}}^*$ with

$$\tilde{k}_i^* = \begin{cases} \widetilde{k}_i, & \left|\widetilde{k}_i\right| \geq k_{\text{th}} \\ 0, & \text{otherwise} \end{cases}. \tag{6}$$

2.2.3 Quality measures compression rate r_c and relative approximation error r_ε

The compression rate r_c can then be defined as the ratio

$$r_c = 1 - \frac{\left\|\widetilde{\mathbf{k}}^*\right\|_0}{n}. \tag{7}$$

Hence, the choice of the threshold k_{th} determines the compression rate r_c. Moreover, different compression rates lead to different relative approximation errors

$$r_\varepsilon = \frac{\varepsilon}{\|\mathbf{g}\|_2} = \frac{\|\mathbf{g} - \widetilde{\mathbf{g}}^*\|_2}{\|\mathbf{g}\|_2}, \tag{8}$$

where $\mathbf{g}$ and $\widetilde{\mathbf{g}}^*$ are the concatenations of the columns of the images $\mathbf{G}$ and $\widetilde{\mathbf{G}}^*$, respectively. The corresponding reconstructions $\widetilde{\mathbf{g}}^*$ are shown in figure 2.

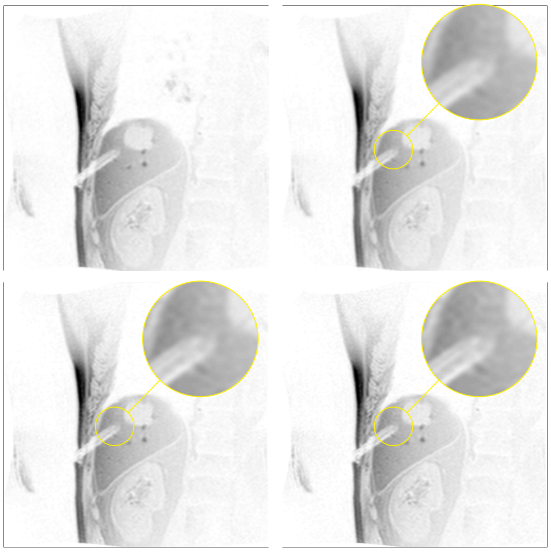

Figure 2: Original image $\mathbf{g}_1$ and images $\widetilde{\mathbf{g}}_1^*$ reconstructed from the ℓ_0-norm minimized $\mathbf{k}$-space $\widetilde{\mathbf{k}}_1^*$ with different relative approximation errors $r_\varepsilon = \{5, 3, 2\}$ %.

3 Results

In table 1, the compression rates r_c and the corresponding relative approximation errors r_ε for each image $\mathbf{g}_1$-$\mathbf{g}_3$ are listed. The compression rate and the relative approximation error have been calculated according to (7) and (8), respectively.

relative approximation error	$\mathbf{g}_1$	$\mathbf{g}_2$	$\mathbf{g}_3$
$r_\varepsilon \approx 10\,\%$	97.0 %	79.3 %	94.6 %
$r_\varepsilon \approx 5\,\%$	92.4 %	63.2 %	82.6 %
$r_\varepsilon \approx 3\,\%$	90.0 %	57.7 %	77.9 %
$r_\varepsilon \approx 2\,\%$	88.2 %	41.1 %	70.3 %

Table 1: Results of the approximated ℓ_0-norm minimization (6) applied to the synthetically generated $\mathbf{k}$-space data $\mathbf{k}_1$-$\mathbf{k}_3$. The compression rates r_c [%] are listed for equal relative approximation errors $r_\varepsilon = \{10, 5, 3, 2\}$ %.

4 Discussion

The method investigated here, yields highly compressed representations $\widetilde{\mathbf{k}}$ of the raw data $\mathbf{k}$ with compression rates r_c depending on the image content. When ℓ_0-norm-minimum-approximation (6) is performed after ℓ_1-norm compression, the resulting $\widetilde{\mathbf{k}}^*$ is an approximation of the ℓ_0-norm minimum of $\mathbf{k}$, i.e. has approximately the highest number of zero elements. Therefore, ℓ_0-norm minimization (3) yields $\mathbf{k}$-space-approximations, which contain the image information in a minimal number of measurements. From figure 2 it can be seen that the main effect of the relative approximation error is the resolution of

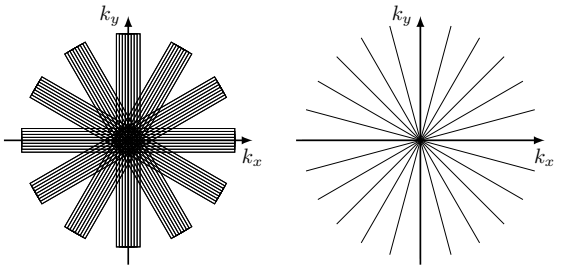

(a) (b)

Figure 3: Non-cartesian **k**-space sampling schemes. (a): PROPELLER, (b): radial.

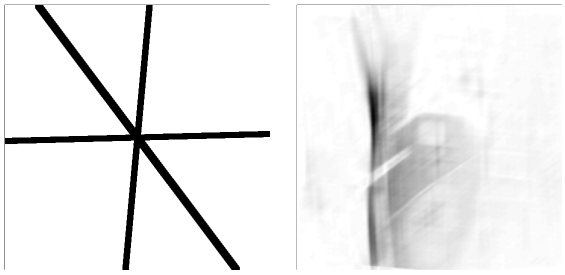

(a) (b)

Figure 4: Trajectory for the drastically reduced **k**-space $\widetilde{\mathbf{k}}_1^{\mathrm{P}}$ (a) and the reconstructed image $\widetilde{\mathbf{g}}_1^{\mathrm{P}}$ (b). The compression rate of $r_{\mathrm{c}} = 94.4\,\%$ leads to a relative approximation error of $r_{\varepsilon} \approx 4\,\%$.

the images. A greater relative approximation error leads to a more blurry image.

The main objective of this work was to determine relevant **k**-space data in order to accelerate the imaging process. The resulting **k**-space vectors $\widetilde{\mathbf{k}}^*$ contain only the most important entries for obtaining a specific relative approximation error. However, such an arbitrary **k**-space sampling does not yield a reduction in imaging time. It can be observed that the entries of $\widetilde{\mathbf{k}}^*$ do not differ from the corresponding entries of **k**. Moreover, such vectors cover similar **k**-space-patterns as MRI acquisition techniques like PROPELLER [3] (**P**eriodically **R**otated **O**verlapping **P**aral**lEL** **L**ines with **E**nhanced **R**econstruction) and radial acquisition (see figure 3). Therefore, this compression method could already be applied during the measurement process by adapting the observed contribution of required sampling points to these non-cartesian **k**-space trajectories. Especially for interventional MRI, this sampling schemes could be advantageous, since e.g. a biopsy needle is represented in the raw data as a radial spoke (cf. PROPELLER blades) with certain properties.

One example of an image $\widetilde{\mathbf{g}}^{\mathrm{P}}$ reconstructed from a drastically reduced **k**-space $\widetilde{\mathbf{k}}^{\mathrm{P}}$ is shown in figure 4. Here, the **k**-space sampling scheme has been built by approximately adapting the ℓ_0-norm minimized vector $\widetilde{\mathbf{k}}^*$ to a PROPELLER-like sampling pattern ($\widetilde{\mathbf{k}}_1^{\mathrm{P}}$) and solely using these data for the reconstruction of $\widetilde{\mathbf{g}}_1^{\mathrm{P}}$. The image quality of this image $\widetilde{\mathbf{g}}_1^{\mathrm{P}}$ is low comparing to the image quality of the image $\widetilde{\mathbf{g}}_1^*$ (see figure 2). The reason for this is that too much information is neglected. However, in interventional MRI, the image content does not change dramatically from one image to the next, since the main difference in the images is due to the needle movement. Thus, the missing data could be replaced by previously recorded data:

1. record one initial **k**-space
2. determine relevant PROPELLER blades
3. record **k**-space data along this sampling scheme
4. replace missing data by initial **k**-space data
5. reconstruct image.

The image series in figure 5 gives an example for the application of this method to interventional MR images.

Acknowledgement

This work was funded by the Federal State North Rhine-Westphalia in the IuK & Gender Med.NRW program, grant no. 005-GW02-052.

References

[1] E. Candès and J. Romberg. Recovery of sparse signals via convex programming. Technical report, Stanford University, 2005.

[2] E. Candès, J. Romberg, and T. Tao. Robust uncertainty principles: Exact signal reconstruction from highly incomplete frequency information. *IEEE Trans. In-form. Theory*, 52:489–509, 2004.

[3] G. Glover and J. Pauly. Projection reconstruction techniques for reduction of motion effects in mri. *Magn Reson Med*, 28:202–213, 1992.

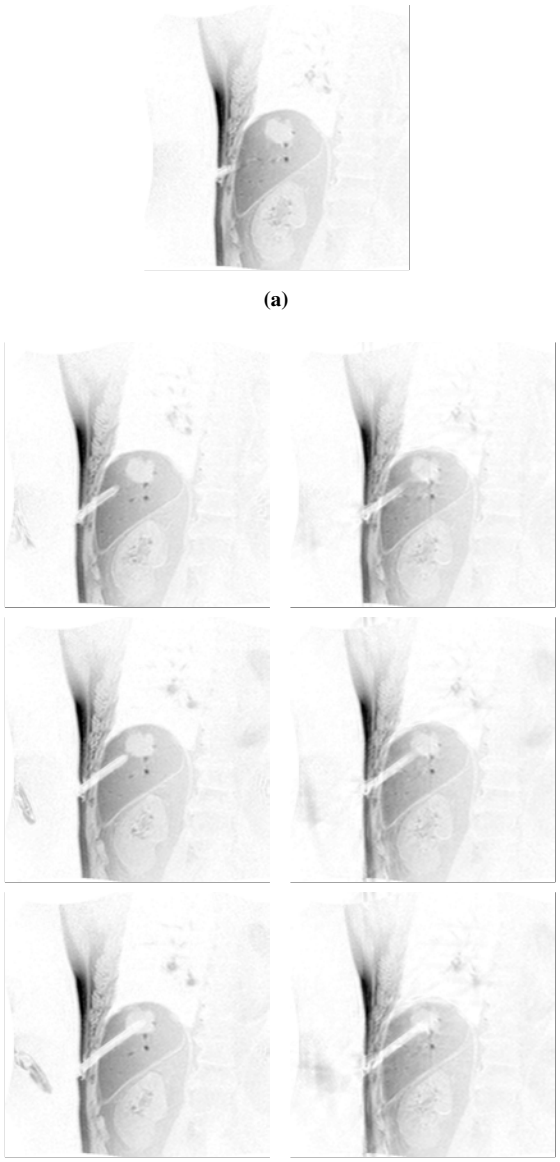

(a)

(b) (c)

Figure 5: Image series of an MR-guided liver biopsy. The top image (a) shows the initial image which provides the initial $\mathbf{k}$-space data. (b): original images $\mathbf{g}$. (c): approximated images $\widetilde{\mathbf{g}}$, reconstructed from the combination of the initial $\mathbf{k}$-space and data recorded with the sampling scheme of figure 4a.

Vascular structure tracking in intraoperative 3D ultrasound data during brain tumor resection

E Ilunga Mbuyamba, Innovation Center Computer Assisted Surgery (ICCAS), Universität Leipzig, Leipzig, Germany, e.ilungambuyamba@ugto.mx
D Lindner, University Hospital, department of Neurosurgery, Universität Leipzig, Leipzig, Germany
F Arlt, University Hospital, department of Neurosurgery, Universität Leipzig, Leipzig, Germany
A Müns, University Hospital, department of Neurosurgery, Universität Leipzig, Leipzig, Germany
J Meixensberger, University Hospital, department of Neurosurgery, Universität Leipzig, Leipzig, Germany
C Chalopin, Innovation Center Computer Assisted Surgery (ICCAS), Universität Leipzig, Leipzig, Germany

Introduction

Intraoperative ultrasound imaging is commonly used in brain tumor surgery to investigate the possible presence of residual tumors after removing the tumor. In B-mode ultrasound images tumor remnant in the resection cavity is difficult to distinguish from other hyperechogenic structures. The use of an ultrasound contrast agent enables to highlight the residual tumors, but also the vascular structures which have to be therefore extracted in the images.

Methods

The patient image dataset includes a preoperative contrast T1 MR data and 3D intraoperative contrast enhanced ultrasound (3D-iCEUS) data acquired before and after tumor resection. Because of the low signal to noise rate the automatic extraction of the vascular stuctures in the 3D-iCEUS data is complex. Therefore, the user defines a region of interest in the preoperative MR data including a blood vessel perfusing the tumor. Using a rigid registration method this pattern is searched in the 3D-iCEUS data before resection within a larger region because of the brain shift. The detected blood vessel becomes then the new pattern to identify the same vascular structure in the 3D-iCEUS data after resection. The extracted blood vessels are finally segmented using a vesselness method and visualized.

Results

Our method was tested on data of three patients overcoming a brain tumor operation. It was validated by registering the preoperative MR data with the 3D-iCEUS data using the transform matrix obtained in the registration method. The correct overlapping of anatomical structures, especially the brain tumor in the 3D-iCEUS data before resection, was visually checked.

Conclusion

Despite the small size of the vascular structures and the low signal to noise rate of the ultrasound image it was possible to track the blood vessels in the patient data. The interactive selection of the region of interest can be performed during the operation planning step.

Estimation of the Brain Network for Perception of Body Movement with Intermediate Nodes

H. Perkunder*, helen.perkunder@informatik.hu-berlin.de
G. Ivanova*, givanova@informatik.hu-berlin.de
*Department of Computer Science, Humboldt Universität zu Berlin, Berlin, Germany.

Introduction

In recent research the brain connectivity is modelled as a complex network. For this purpose functional and structural networks can be estimated with functional (fMRI) and diffusion weighted imaging (dMRI), respectively. But activated regions from fMRI are often not directly structurally connected. We introduce a method that fuses functional and structural networks using intermediate nodes.

Methods

The potential intermediate nodes are modelled as voxels that a large number (n) of tracks run through. They can be interpreted as local hubs in the structural network. Tracks are reduced to those that run through functional or intermediate nodes. Then the adjacency matrix of all nodes is calculated, followed by the calculation of shortest paths between the functional nodes. The coordinates of 14 published functional nodes involved in the perception of body motion were nonlinear transformed to the dMRI space of a randomly chosen subject from a multimodal data pool and used for selection of tracks.

Results

We calculated the networks for n=200 to n=100, with descending steps of 25. The number of intermediate nodes increased with decreasing number of tracks. From a total of 91 potential connections only 13 direct connections existed, if no intermediate nodes were used. With n=100, all but 2 regions were interconnected with a maximum of 6 intermediate nodes, mean distance of 3.8 between functional nodes; with n=75, all but one region were connected, maximum of 6 intermediate nodes, mean distance 3.3.

Conclusion

Structural and functional networks can be fused by a small number of intermediate nodes. The physiological meaning of intermediate nodes must be examined in a next step, for instance by integration in the analysis of fMRI data.

Phantom for testing of MRI image artefacts of interventional devices in MRI

R. Bahadir[1,2], M. Choli[2], K. Skopnik[2], J. Watzlaw[2], G. Schaefers[2], [1]Medical Engineering, Westphalian University of Applied Sciences, Gelsenkirchen, Germany, [2]MR:comp GmbH, Testing Services for MR Safety & Compatibility, Gelsenkirchen, Germany, info@mrcomp.com

Introduction

The weighted average carcinosis are breast and prostate cancer [1]. A procedure of high accuracy has enormous relevance in clinical routine to diagnose cancer in early stadium. Biopsies made under ultrasound guidance typically remove more tissue than nessary. The alternative approach of using magnetic resonance imaging (MRI) is advantageous due to better resolution. In cooperation with the Westphalian University of Applied Sciences, we are developing a method for biopsies guided by real-time MRI, where the MR image artefact of the biopsy needle is used for needle tracking. In the current established standard test method ASTM F2119 [2], a phantom is requested that facilitates the investigation of MR image artefacts of passive implants for worst-case detection. In our approach, we combined this request with the need for determining the basic needle artefact parameters for various realistic cases of needle orientation between the ‘best-case’ and the ‘worst-case’.

Methods

An acrylic phantom has been designed in order to evaluate MR image artefacts of needles with simultaneously offering a high degree of freedom of needle orientation. We faced the challenging electromagnetic environment of MRI by using fully nonmagnetic and nonconductive materials. A cylinder system serves as a precise angular adjustment of the needle in two directions.

Results

The MRI suitable phantom enables the investigation of MR image artefacts of different types of biopsy needles. Due to its innovative design, the needle can be moved to well defined and realistic orientations in space related to the B_0 field direction while meeting the needs of the recognized ASTM test method for worst-case artefact detection.

Conclusion

Measurements using the phantom can demonstrate the behaviour of MR imaging artefacts of different needles and different realistic needle orientations. This innovative solution in needle alignment and MR image artefact measurement results in identifying the exact location of the needle.

References

[1] „Krebs in Deutschland 2009/2010“, 9. Ausgabe, Robert Koch-Institut (Hrsg) und die Gesellschaft der epidemiologischen Krebsregister in Deutschland e.V. (Hrsg), Berlin, 2013
[2] ASTM Standard F2119-07, Reapproved 2013, ”Standard Test Method for Evaluation of MR Image Artifacts from Passive Implants”, ASTM International, West Conshocken, PA, 2013, DOI: 10.1520/F2119-07R13, www.astm.org

Acknowledgement

The authors acknowledge the government of North Rhine-Westphalia (IuK & Gender Med.NRW, grant no. 005-GW02-052B) for financial support.

Market potential of MR-compatible guidewires and assessment of MR safety and compatibility

G. Uihlein, University Of Applied Science, Aalen, Germany, georg.uihlein@gmail.com
G. Schaefers, MR:comp GmbH, Services for MR safety & compatibility, Gelsenkirchen, Germany, info@mrcomp.com

Introduction

In the center of the research stands a newly developed innovation of the *EPflex Feinwerktechnik GmbH.* It's a guidewire for minimally invasive surgery, which can be used inside an MRI Scanner.
Aim of the research was finding out the product's market potential (MP) and definig the innovation-driven market strategy.
Also MR-compatibility assessment is very important, starting already in the design for MR-conditional products acc. to IEC62570 (ASTMF2503-13).

Methods

First, a Stakeholder analysis as well as a SWOT analysis of the product were made in order to receive a clear view of the actual situation. After that, the MP= Z x a_z was calculated by multiplying the number of potential users (Z) with amount of products per year they are willing to buy (a_z). The difficulty was to find out all users interested in the product. Besides desk research, an online survey was carried out to gain the needed data.
Designing and testing new innovative products is planned according to standards like IEC 62570 including all necessary MR-related interactions like force, torque, RF heating and MR artifacts. (ASTM-F2052; F2213; F2182; F2119; ISO/TS10974).

Results

The total market potential for an MR-compatible guidewire is 3,7 million pieces per year, valid for a fully developed market. At the moment, a maximum sale of 121,000 pieces per year is realistic.
An early stage MR compatibility strategy, based on test methods, results into the feasible entry stage into device development.

Conclusion

Based on the study, an MR-compatible guidewire is able to grow to a successful niche product asked by potential customers showing serious interest, especially in the field of cardiovascular/ peripheral vascular interventions.
In the early phases of the innovation, considering MR-related design as well as market-related demands is important to develop both, a safe and successful MR product.

Otoendoscopic Visualization of Tympanoscopic Landmarks for Middle Ear Interventions and Robot Assisted Direct Cochlear Access

Patrick Dubach[1], Marco Caversaccio[2], Stefan Weber[3], Gero Strauß[14]

[1] BMBF-Innovation Center Computer Assisted Surgery ICCAS, University of Leipzig, 04103 Leipzig, Germany, patrick.dubach@insel.ch
[2] Department of Otorhinolaryngology, Head and Neck Surgery, Inselspital, Bern University Hospital, Switzerland
[3] ARTORG Center for Biomedical Engineering Research, University of Bern, 3008 Bern, Switzerland
[4] International Reference and Development Center for Surgical Technology (IRDC), Leipzig, Germany

Abstract

Introduction

Endoscopy established itself as alternative to traditional (often indirect mirror based) microscopic tympanoscopy and became strongly promoted for various endoscopic middle ear procedures. In order to brigde middle ear and inner ear function by prosthetic surgery, an optimal visualization of important areas of the transition zones between middle and inner ear becomes of special interest; i.e. stapes footplate, round window niche. This study evaluates the potentials of today´s available endoscopic systems for direct transcanal tympanoscopy.

Methods

Under standardized conditions, trained otologists rated independently the degree of visualization (in % area of interest) and the digital image quality (by Visual Analogue Scale) for systematic transcanal tympanoscopy in human formalin fixed temporal bone. In addition to a digital camera and image processing (SPIES, Karl Storz™) the microscopic (Zeiss™), 1.3mm sialendoscopic and 2.7mm otoendoscopic (Karl Storz™) and Chip on Tip (COT) imaging and film data have been used to evaluate transcanal middle ear inspection of microsurgical target structures; especially surgical gateways to the inner ear (e.g. round windown niche for cochlear implant (CI) insertion or stapes footplate for passive and active hearing prosthesis insertion).

Results

Compared with transcanal microscopic inspection, the visualization with endoscopes was rated as more complete for the sinus tympani, facial recess, Eustachian tube orifice, and epitympanum. Digital image processing may help in correction of adverse light effects especially in the Eustachian tube area. For structures out of direct line of sight, best picture quality was achieved by digital and rod lens endoscopy. Optimal results were achieved by the microscope in the regions accessible with straight line of sight only. On the other hand, 45° rod lense endoscopes showed best results for hidden regions with angulated view. Adequate endoscopic visualization of the stapes footplate and the round window niche as well as monitoring of the transtympanic part of robot assisted direct cochlear access in cadaver heads was feasible.

Conclusion

Endoscopes offer a portable and low cost alternative to microscopes for minimal invasive transcanal tympanoscopy and interventions especially in hidden recesses od the middle ear. (i.e. round window niche and stapes footplate for hearing implant surgery or sinus tympani and facial recess to exclude hidden ear disease). Best picture quality was achieved by digital rod lens and the microscope. Digital endoscopic image processing may in the Eustachian tube region improve inspection even in adverse light effects. The microscope showed good results when objects with straight line of sight were inspected. On the other hand, endoscopy may not only improve visualization of many structures and maneuvers by an angled view but provides also for detailed and sharp picture quality. Progress in endoscopic and especially camera chip technology will allow for much smaller scaled tools which can be integrated in robot systems reducing the access paths and thus invasive exposure for interventions. An example of endoscopic visualization for simulated robot assisted CI is given.

This study was supported by the Bangerter-Rhyner Foundation and the SSMBS Schweizerische Stiftung für Medizinisch Biologische Forschung P3_SMP3 148371/1.

1 Introduction

In order to evaluate the microanatomy of the complex middle ear structures for otosurgery[1], various microscopic techniques (e.g. reversible canal wall down operations) have been proposed[2,3]. Even indirect mirror based[4,5,6] microscopic techniques have been described to compensate for the inherent need of straight line of sight and restriction by the tunnel like view of the microscope. Alternatively, endoscopic systems have been developed to achieve more comprehensive views into hidden anatomical recesses. Moreover, with their angulated visual axis and a wide viewing angle (opening like a funnel) endoscopy became strongly promoted as complementary tool[7] for various therapeutic middle ear intervention with specific indications[8,9,10] and even for CI surgery[11].

This study evaluates the potentials for transcanal tympanonoscopy comparing today´s most common endoscopic system (rod lense and fiberoptic digital camera systems and camera chip on the endoscope tip). In addition to the degree of visibility adressed by previous studies[12,13,14,15], we also evaluated the picture quality as subjectively perceived by the individual surgeon in order to define its role in image guided otologic therapy[16]. As an example, a potential future application of miniaturized chip on tip endoscope is tested in a pilot experiment simulating direct tunnel access as described with prototypes for robot assisted direct cochlear implantation1[17,18,19.20.21].

2 Methods

For transcanal diagnostic tympanoscopy (Fig 1), the conventional microscope OPMI Vario™ by Zeiss (Mic) and the following Karl Storz instruments have been compared: 2.7mm diameter 45° angled rod lense without (45) and with SPIES™ camera system (45S), 1.3mm diameter flexible sialendoscope (Sial) and a prototype of chip on tip (COT) camera system. For illumination a Xenon light source has been used and the middle ear was inspected raising a posterior based tympanomeatal flap. Videodocumentation of systematic tympanonscopy was recorded for the traditional landmarks in middle ear surgery[22,23,24] in the following order: 1) promontory:P, 2) entrance to the round window niche: RWN, 3) stapes footplate: SF, 4) sinus tympani: ST, 5) facial recess: FR, 6) epitympanon: ET (i.e. tensor tendon, incudo-malleolar joint), 7) Eustachian tube and supratubal air cells: ET and 8) hypotympanon: HT (Fig 1). Human temporal bones were used because no temporarily available artificial model could match with with it in the pre-experiments. The study was performed according to the ethical guidelines of the Swiss Academy of Medical Sciences on individuals who had provided written consent to dedicate their body to medical research and educational training purposes at the University of Bern, Switzerland on none-diseased formaline fixed human temporal bones . Data for Mic, 45 and 45S were recoreded by AIDA™ sytem. For Sial with digital filter A and for COT recording by the Tele Pack X™ system by Karl Storz has been performed. Reassessing the most important landmarks described in previous visualization studies[11,12,13,14], six ENT surgeons evaluated the still picture of each landmark and the dynamic film sequence of the tympanoscopy in randomized order on a 42'' Wide View™ monitor by Karl Storz. The surgeons had a median experience in ear surgery of 5 years (range 2 to 23years) and rated the degree of visibility of the landmarks in % of the area of interest using still images (1920x1080pixels for microscope and rodlense systems; 1024x768 pixels for sialendoscope and COT). Second, overall picture quality was measured evaluating dynamic examination on film (1920x1080 pixels,29pps for microscope and rodlense systems; 640x480 pixels,25pps for sialendoscope and COT). Overall picture quality was defined as the individually perceived sharpness of the details rating their perception of sharpness with a vertical pencil mark on a scale from 0 to 10cm (0: unusable, 10: excellent picture quality).

Figure 1 Transcanal view into left side ear after tympanic membrane removal with systematic tympanendoscopic evaluation of key microsurgical target structures

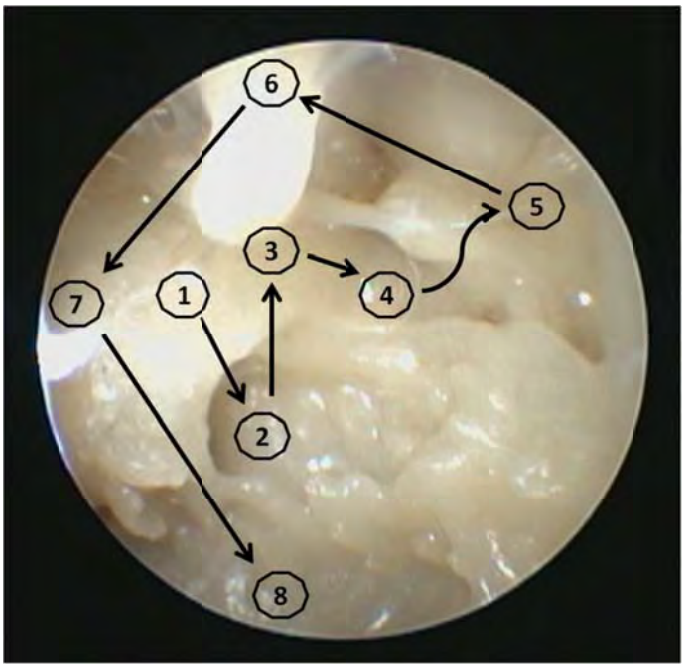

3 Results

For middle ear landmarks visible with a straight line of sight along the external ear canal axis, most complete visualization was achieved by 45,45S and Mic systems. In hidden areas of the SF, ST, FR, EP and ET, endoscopes with 45° angeled visual axis were superior to the microscop and also to the microscope combined with indirect mirror inspection (SF,ST,FR,EPI,ET, HT).

Figure 2 Boxplot of degree of visualization in % for specific endoscopic system (45, 45S, Sial, COT, Mic) grouped according specific landmark inspected.

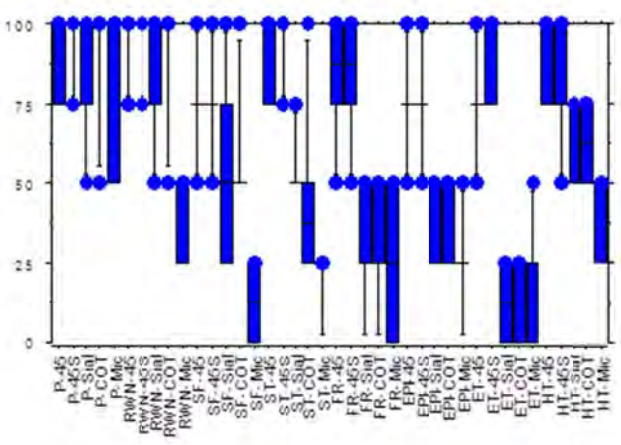

Picture quality was significantly dependent on the tympanoscopic system used ($p<0.05$, Friedman test). Although partial visualization of most middle ear structures was feasible with Mic, Sial and COT, the picture produced by these techniques were far from excellent and rated worst for the fiberoptic transmission by the Sial (Fig 3).

Figure 3 Individual rating of overall picture sharpness on dynamic film recordings of transcanal tympanoscopy. Box Plots of ratings on visual analogue scale ranging from 0 to 10cm (0: Absolutely unusable and 10cm:excellent).

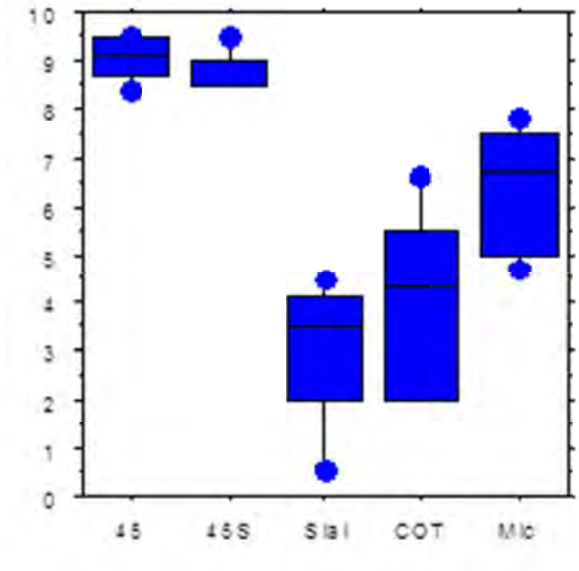

For the RWN as surgical target structure for direct cochlear access , best compromise between extent of visualization and picture quality was provided by endoscope with 45° visual axis and by the COT. In a pilot experiment we used transcanal COT to monitor planned direct cochlar access (Image 1A) and to visualize the transtymanic progress of the burr along the direct cochlear access track (Image 1B). Wide Viewing angle and the large depth of focus allowed comprehensive monitoring of the transtympanic part of the procedure.

Image 1: Example of a wide field of view by miniaturized COT endoscope for visualization of the complete planned burr track (A) Example of wet lab simulation of robot assisted direct cochlear implant insertion (B) in a human temporal bone.

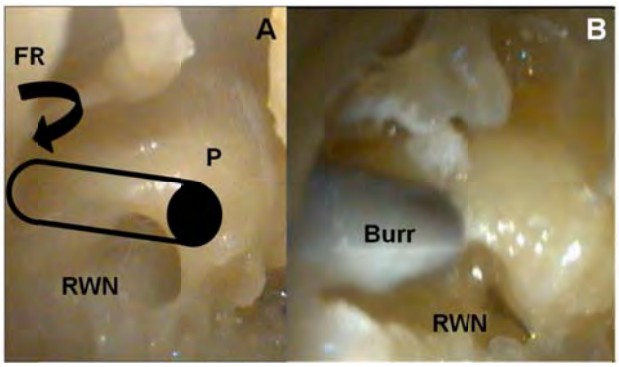

4 Conclusions

Previous studies described an advantage of a 30° and 70° endoscopes[25] compared to the microscope for complete visualization of important middle ear structures hidden in angled corners (ST, RF,SF..) from direct straight line of sight. These studies were often limited to one specific endoscopic system (rod lense or fiberoptic) and studied only the endpoint of degree of visualized area. Results of 1.7mm diameter 0°, 30° and 90° [13] as well as 4mm 0° and 2.7mm 70° [15]endoscopes or 0.4mm 0.7mm and 1mm fiberscopes[8] were thus methodologically difficult to compare. In addition to these previous "visualization studies"[12] we evaluated systematically a microscopic and four of the mainly used endscopic systems focusing especially also on picture quality.The degree of visibility for landmarks out off the straight line of sight was insufficient or unusuable for the mirror image and microscope and only of restricted use for endoscopic systems with 0° visual axis (Sial, COT). The 45° angled endoscopes (45, 45S) provided best results and were much easier to guide through the middle ear space because of better orientation than previously described 70° or 90° endoscopes.

Best picture quality was either provided by the microscope when direct inspection without the need of a microscopic mirror was possible (P,RWN) or by the rod lens endoscopic systems. The 45 and 45S provided better picture quality especially for ST, SF, FR, EPI, HT. In addition inspection of very restricted regions of the EPI and ET, inspection with digitial image processing SPIES™ were perceived by some surgeons as better illuminated .

Future development will address smaller endoscopes with variable angle or flexible steerable tip as well as chip on tip solutions. These new developments will greatly facilitate otoscopic procedures as outlined in suggested indications and might well promote and support the applications

of minimal invasive robot assisted ear surgery such as direct cochlear access cochlear implantation.

4 References

[1] Goodhill V. Circumferrential tympano-mastoid acess. The sinus tympani area. Ann Otol Rhinol Laryngol 1973;82:547.54.

[2] McElveen JT Jr, Hulka GF. Reversible canal wall down tympanomastoidectomy. An alternative to inctact wall and canal wall down mastoidectoimy procedures. Am J Otol 1998;19:415-419.

[3] Pickett BP, Cail WS, Lambert PR. Sinus tympani: Anatomic considerations, computed tomography and discussion of retrofacial approach for removal of disease. Am J Otol 1995;16:741-50.

[4] Zini C. La microtympanoscopie indirecte. Revue de laryngologie otologie-rhinologie 1967; 9-10 :736-738.

[5] Buckingham RA. Antrum and attic inspection mirror. Trans Am Acad Ophthalmol Otolaryngol 1968;72(1):115-6.

[6] Yanagihara N. A surgical treatment of cholesteatoma: problems in idications and technique. In: Sade J (Ed.) Cholesteatoma and mastoid surgery. Proceedings of the Second International Conference. Kluger Amsterdam. 1982. 483-490.

[7] Thomassin JM. Duchon-Doris JM, Emeran B, Rud C, Conciatori J, Vilcoq P. [Endoscopic sugery oft he ear – First assessment]. Ann Oto-Laryngol 1990;107:564-570.

[8] Poe DS, Rebeiz EE, Pankratov MM, Shapshay SM. Transtympanic endoscopy of the middle ear. Laryngoscope 1992;102:993-6.

[9] Tarabichi M. Transcanal endoscopic management of cholesteatoma. Otol Neurotol. 2010;31(4):580-8.

[10] Badr-El-Dine M, James AL, Panetti G, Marchioni D, Presutti L, Nogueira JF.Instrumentation and technologies in endoscopic ear surgery. Otolaryngol Clin North Am. 2013;46(2):211-25.

[11] Marchioni D, Grammatica A, Alicandri-Ciufelli M, Genovese E, Presutti L Endoscopic cochlear implant procedure. 3] Eur Arch Otorhinolaryngol. 2014 May;271(5):959-66.

[12]Rehl RM, Oliaei S, Ziai K, Mahboubi H, Djalilian HR. Tympanomastoidectomy with otoendoscopy. Ear Nose Throat J 2012;12:527-532.

[13] Karhuketo TS, Puhakka HJ, Laippala PJ. Endoscopy of the middle ear structures. Acta Otolaryngol 1997;529:34-39.

[14] Karhuketo TS, Laippala PJ, Puhakka HJ, Sipilä M. Endoscopy and Otomicroscopy in the Estimation of Middle Ear Structures. Acta Otolaryngol 1997;117:585-589.

[15] Bowdler DA, Walsh RM. Comparison of the otoendoscopic and microscopic anatomy of the middle ear cleft in canal-wall up and canal-wall down temporal bone dissections. Clin Otolaryngol Allied Sci 1995;20:418-22.

[16] Dubach P, Bell B, Weber S, Caversaccio. “Image Guided Otorhinolaryngology.” In: Jolesz F.Intraoperative Imaging and Image Guided Therapy. Stuttgart- New York. Springer Publishers; 2014:845-856.

[17] Kratchman LB, Blachon GS, Withrow TJ, Balachandran R, Labadie RF, Webster RJ 3rd. Design of a bone-attached parallel robot for percutaneous cochlear implantation. IEEE Trans Biomed Eng. 2011 Oct;58(10):2904-10

[18] Miroir M, Nguyen Y, Szewczyk J, Sterkers O, Bozorg Grayeli A.Design, kinematic optimization, and evaluation of a teleoperated system for middle ear microsurgery. ScientificWorldJournal. 2012;Epub 2012 Aug 13.

[19] Nguyen Y[1], Miroir M, Vellin JF, Mazalaigue S, Bensimon JL, Bernardeschi D, Ferrary E, Sterkers O, Grayeli AB. Minimally invasive computer-assisted approach for cochlear implantation: a human temporal bone study. Surg Innov. 2011 Sep;18(3):259-67.

[20] Majdani O, Rau TS, Baron S, Eilers H, Baier C, Heimann B, Ortmaier T, Bartling S, Lenarz T, Leinung M. A robot-guided minimally invasive approach for cochlear implant surgery: preliminary results of a temporal bone study. Int J Comput Assist Radiol Surg. 2009 Sep;4(5):475-86.

[21] Bell B, Gerber N, Williamson T, Gavaghan K, Wimmer W, Caversaccio M, Weber S. In vitro accuracy evaluation of image-guided robot system for direct cochlear access. Otol Neurotol. 2013;34:1284-90.

[22] Proctor B. Surgical anatomy of the posterior tympanum. Ann Otol Rhinol Laryngol 1969;78:1026-1040.

[23] Thomassin JM, Danvin JB, Collin M. Endoscopic anatomy oft he posterior tympanum . Rev Laryngol Otol Rhinol 2008;129:239-243.

[24] Marchinoi D, Molteni G, Presutti L. Endoscopic anatomy of the middle ear. Indian J Otorhinolaryngol Head Neck Surg 2011;63:101-113.

[25] The Swiss Academy of Medical Sciences. Verwendung von Leichen und Leichenteilen in der medizinischen Forschung sowie Aus-, Weiter- und Fortbildung – Empfehlungen der SAMW. November 27, 2008. Available at http://www.samw.ch/de/Publikationen/Empfehlungen.html. Accessed 23r April 2014

[26] Rosenberg SI. Endoscopic otologic surgery. Otolaryngol Clin North Am 1996;29:291-93.